Smart Structures and Systems, *Vol. 15, No. 6 (2015) 1393-1410*
DOI: http://dx.doi.org/10.12989/sss.2015.15.6.1393

Hinge rotation of a morphing rib using FBG strain sensors

Monica Ciminello[*1], Salvatore Ameduri[1a], Antonio Concilio[1b], Domenico Flauto[2c] and Fabio Mennella[3d]

[1]C.I.R.A.- Italian Aerospace Research Center, Smart Structures Lab, Via Maiorise 81043, Capua (CE), Italy
[2]University of Palermo, Aerospace Engineering Dept - Viale delle Scienze 90128, Palermo, Italy
[3]University of Napoli "Federico II", Composite Material Dept - P.le Tecchio 80100, Napoli, Italy

(Received September 3, 2013, Revised February 2, 2014, Accepted February 12, 2014)

Abstract. An original sensor system based on Fiber Bragg Gratings (FBG) for the strain monitoring of an adaptive wing element is presented in this paper. One of the main aims of the SARISTU project is in fact to measure the shape of a deformable wing for performance optimization. In detail, an Adaptive Trailing Edge (ATE) is monitored chord- and span-wise in order to estimate the deviation between the actual and the desired shape and, then, to allow attaining a prediction of the real aerodynamic behavior with respect to the expected one. The integration of a sensor system is not trivial: it has to fit inside the available room and to comply with the primary issue of the FBG protection. Moreover, dealing with morphing structures, large deformations are expected and a certain modulation is necessary to keep the measured strain inside the permissible measure range. In what follows, the mathematical model of an original FBG-based structural sensor system is presented, designed to evaluate the chord-wise strain of an Adaptive Trailing Edge device. Numerical and experimental results are compared, using a proof-of-concept setup. Further investigations aimed at improving the sensor capabilities, were finally addressed. The elasticity of the sensor structure was exploited to enlarge both the measurement and the linearity range. An optimisation process was then implemented to find out an optimal thickness distribution of the sensor system in order to alleviate the strain level within the referred component.

Keywords: smart aircraft structures; Fiber Bragg Grating sensor; rotation angle; shape reconstruction

1. Introduction

There are many variables that can affect a civil aircrafts performance. Basically, it is rare that an aircraft flies at its design point. The weight changes constantly during a single mission, as the fuel burns; moreover, the weight itself cannot be predicted "a priori" depending on the number of passengers that actually fly. Moreover, transfer flight, short or long range flights have different characteristics. The assigned routes themselves can affect important parameters like the attitude and the dynamic pressure. It may be estimated that the lift coefficient may vary in a range of

*Corresponding author, Ph.D., E-mail: m.ciminello@cira.it
[a] Ph.D., E-mail: s.ameduri@cira.it
[b] Ph.D., E-mail: a.concilio@cira.it
[c] Student, E-mail: domenicoflauto@gmail.com
[d] Student, E-mail: fabiomennella@libero.it

http://www.techno-press.org/?journal=sss&subpage=8 ISSN: 1738-1584 (Print), 1738-1991 (Online)

almost one order of magnitude during life-long aircraft operations. Because of that, the use of variable shape wings (morphing wings) can be of extreme interest as studied by Pecora *et al.* (2012), and Ameduri *et al*. (2012). A way to attain the desired deformations within the necessary structural safety factors is to implement Adaptive Trailing Edge (ATE) devices, like the one being developed inside the SARISTU Project, sponsored by the EU inside the VII Research Framework Programme, (http://www.saristu.eu).

A key aspect to realize flyable ATE devices is to assure the specified displacements under variable loads. The design of the sensor network is driven by the necessity of providing the shape control system with continues and widely distributed information over the region of interest. The proposed monitoring architecture uses a wide FBG net to meet that requirement and several other constraints. First of all, airplanes should operate under stringent environmental requisites, related to temperature and moisture. The sensors must withstand a temperature interval, ranging from −50°C to +80°C, depending on a number of factors as the geographical stationing location, the altitude, the operating season and so on.

FBG sensors can easily satisfy the needs related to the operating environment if embedded in special patches or coated with polyimide materials. In addition, electric cables use shielding sheaths to avoid susceptibility to electro-magnetic interference and high-intensity radiated fields with a significant increase of the cable weight. Fiber Optic (FO) are still coated and shielded but simply overcomes this problem by using light instead of electric signals. In the field of Smart Structures, FO were proposed for monitoring airflow pressure over smart wings in the mid-1990s, (Jones *et al*. 2006), for health monitoring of morphing airfoils, whether controlled by classical or SMA (Shape Memory Alloys) actuators, as well as multi-parameter skin friction measurements (Duncan *et al.* 2003 and Jung-Ryul *et al.* 2003). FBG have been generally applied in optical sensing as they provide further important advantages, such as high sensitivity, capabilities of multiplexing and networking, wavelength absolute encoding and so on, (Liu *et al.* 2004). Many kinds of FBG-based sensors have been manufactured, (Hui *et al.* 2011), whereas rotational FBG devices are still uncommon in the literature according to the authors' knowledge, (Ciminello *et al.* 2013).

An innovative FBG system is herein proposed to monitor the local hinge rotation of the multi-body skeleton of the referred ATE structure. Moreover, dealing with morphing structures, large deformations are expected and a certain modulation is necessary to keep the measured strain inside the permissible measure range. In what follows, the mathematical model describing the transfer function of the sensor system is firstly described. The sensing device concept is then implemented into a finite element code for validation. Experimental test results are finally presented, using a simple but representative setup.

2. Structural system description

The structural core of the ATE device is made of single degree of freedom (SDOF), segmented ribs. The different segments are hinged to each other and make a sort of chain. Span-wise, the ribs are connected via a number of spars, in order to guarantee a sufficient torsional rigidity. Linear actuators force the segments to rotate, so to increase or decrease the local curvature. Compliant skin assures geometrical surface continuity.

Among the other parameters, information about hinges rotation is necessary to reconstruct the deformed wing shape. The proposed sensor system aims at measuring the relative rotation of two consecutive rib blocks. A simplified schematic of a morphing rib section is sketched in Fig. 1. A single elastic hinge is shown there, connecting a fixed to a rotating section. A bold line represents a generic FO, displayed close to the hinge. This arrangement allows properly modulating the recorded strain, by simply acting on the distance from the hinge center.

Selected sensing element is the well-known FBG. Acting like a sort of "filter", its working principle is based on a change of the refractive index in the FO, consequence of the physical alterations of the FO structure. The FBG reflects then a specific wavelength, the so-called "Bragg wavelength", λ_B, dependent on the grating period, Λ.

$$\lambda_B = 2n_e\Lambda \tag{1}$$

In (1) ne is the refractive index of the fiber core. When a mechanical strain ε is applied to FO, Λ changes and leads to a shift in the reflected Bragg wavelength ($\Delta\lambda_B$). Temperature variations lead to a two-fold effect: a mechanical thermal expansion (with a consequent intrinsic modification of the geometrical Bragg properties) and a microscopic FO structure variation (leading to a change of its general optical properties). Being α_f the thermal expansion coefficient of the bulk material and ξ_f the thermo-optical coefficient, the wavelength shift due to a temperature variation can be derived as

$$\Delta\lambda_B = \lambda_B\left[\left(\alpha_f + \xi_f\right)\Delta T + \left(1 - p_e\right)\varepsilon\right] \tag{2}$$

There, p_e is the photo-elastic constant of the FO and can be derived as follows, having considered the contributions of the Poisson's ratio, *v*, and the components of the strain-optic tensor, p_{11} and p_{12}, (Mohanna *et al.* 2002)

$$p_e = \left(\frac{n_e^2}{2}\right)\left[p_{12} - \upsilon\left(p_{11} + p_{12}\right)\right] \tag{3}$$

Since the temperature change can be neglected in the performed laboratory experiments, Eq. (2) simplifies to

$$\varepsilon = \frac{1}{1 - p_e}\frac{\Delta\lambda_B}{\lambda_B} \tag{4}$$

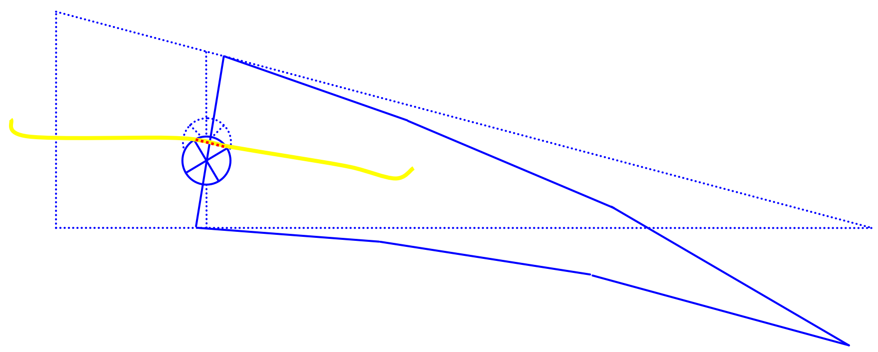

Fig. 1 Schematic of the morphing rib

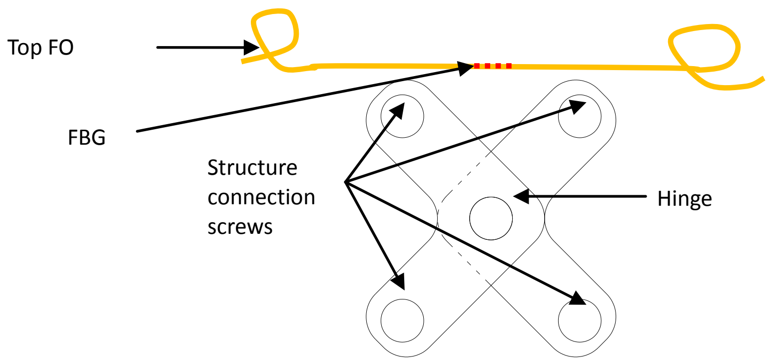

Fig. 2 Schematic of the sensing device

The mechanical structure of the sensing device is sketched in Fig. 2. It consists of two rigid and specular arches hinged at their midpoint to form an “X”. It can be then easily coupled with the reference structure, at the very hinge center. Each arch is then constrained to the aft and fore rib segments, respectively. At a certain point on the top “X” notches are used to clamp the FO. At the fiber center, a 10 mm long FBG is deployed.

FBG sensors used in this application are typically recorded within the core of a single mode optical fiber, just 9 microns in diameter. Together with the outer cladding, these fiber sensors are truly miniature; generally just 0.15 or 0.25 mm in diameter and it is practical to attach the sensing device to the structure under test simply using screws. Following the system geometry, uniform strain can be assumed along the fiber (axial strain). The slipping of the FBG can be then prevented by mechanically clamping the FO to the structural device using glue or special holders.

To avoid damages to the fiber in the compressed region, FO should be opportunely pre-strained using an optical interrogator to set the device to a fixed strain value. This means that the measurement range in the negative strain direction is limited, as it exactly corresponds to the direction and value of the pre-strain. Because the Bragg gratings are located inside the fiber, pre-straining and installing the gauges can cause unwanted damage to the fiber too. Alternative sensor constructions can be considered, for future applications, convenient, robust strain/temperature sensor supplied as a flexible patch (www.smartfibres.com) providing a more robust sensor with a more distributed strain response.

Relaxation effect of the FBG over time was not taken into consideration, as the max allowable deformation of +/-4000 $\mu\varepsilon$ was assumed for the fiber optic and this value is a typical range value for pre-stressed fibers (www.smartfibres.com) and compatible with typical fatigue life requirements (about 10 millions of cycles per ± 5000 $\mu\varepsilon$). Moreover, it was shown that the relaxation of internal stresses profile change is negligible at temperatures of use after 25 years. Hence, the initial internal stress profile, i.e. the refractive index profile, of standard high-tension fiber is not modified during the optical-fiber cable lifetime.

Finally in case of a self-compensation mechanism, top and bottom FOs can be provided. During the rotation of the sensing device, the collocated FBGs are alternatively subjected to opposite tensile and compression loads, respectively and to the same thermal distortions which can be neglected as “common-mode effect” in a similar way to the wavelength shift difference approach (Ciminello *et al.* 2013).

3. Mathematical model

A simple geometrical model can be used to describe the functionality of the proposed sensor system. In Fig. 3 the rib hinge is the centre of the R-radius circle therein sketched, while the arms of the device are drawn as generic diameters, intersecting the circumference at the points A and B and making an angle equal to α_0. The FO is represented by the chord connecting A and B. A relative rotation α of the diameters will cause the segment AB to be stretched (or shrunk) into the segment AC, while its bottom counterpart shrinks (or stretches). Trigonometry leads to

$$AB = 2R\sin(\alpha_0/2) \tag{5}$$

$$AC = 2R\sin((\alpha_0+\alpha)/2) \tag{6}$$

Therefore, implementing the definition of strain

$$\varepsilon = (AC - AB)/AB \tag{7}$$

the following relation is attained

$$\varepsilon = \frac{\sin\left(\frac{\alpha_0+\alpha}{2}\right)}{\sin\left(\frac{\alpha_0}{2}\right)} - 1 \quad \Rightarrow \text{(small values of } \alpha) \Rightarrow \quad \varepsilon \cong \frac{\alpha}{2\tan(\alpha_0/2)} \tag{8}$$

The angle α_0 plays an important role. In fact, according to Eq. (8), α_0 modulates the measured strain .In other words, it is possible to enlarge the measurement range by varying the nominal span of the X-structure. By substituting the Eq. (4) into Eq. (8), under the assumption of quasi-static processes, the Bragg wavelength shift can be also expressed as

$$\Delta\lambda_B = (1-p_e)\left[\frac{\sin\left(\frac{\alpha_0+\alpha}{2}\right)}{\sin\left(\frac{\alpha_0}{2}\right)} - 1\right]\lambda_B \cong (1-p_e)\frac{\alpha}{2\tan(\alpha_0/2)}\lambda_B \tag{9}$$

The corresponding rotational angle sensitivity, S, can be then derived

$$S = \frac{\Delta\lambda_B}{\Delta\alpha} \cong \frac{(1-p_e)\lambda_B}{2\tan(\alpha_0/2)} \tag{10}$$

Without the assumption of small α the sensitivity is given by

$$S = \frac{\Delta\lambda_B}{\Delta\alpha} = \frac{(1-p_e)\left[\frac{\sin\left(\frac{\alpha_0+\alpha}{2}\right)}{\sin\left(\frac{\alpha_0}{2}\right)} - 1\right]\lambda_B}{\Delta\alpha} \tag{11}$$

where $\Delta\alpha$ represents the increment of α.

The Eq. (11) is plotted in Fig. 4. The strain is assumed constant along the fibre, within the AB segment.

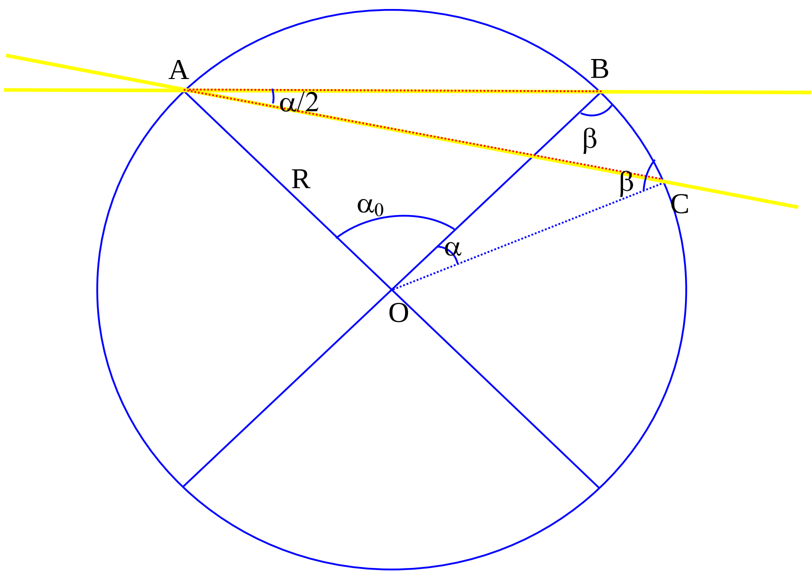

Fig. 3 Geometrical scheme linking hinge rotation to longitudinal strain component

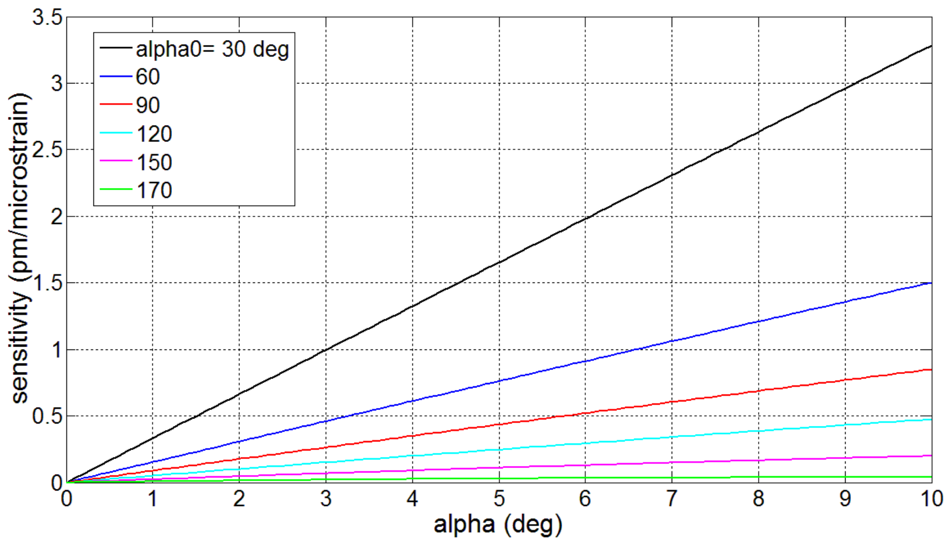

Fig. 4 Schematic of the arch sensing device

4. Numerical and experimental validation

4.1 Numerical process: point rotation by strain detection

In order to validate the analytical transfer function between local strain and rotation described in the previous paragraph, a 2D FE numerical model was firstly set-up.

In detail, the specific morphing rib section was simulated by two rotating blocks, discretized through solid elements. One was clamped along a side) while the second block was linked to the former via a hinge, allowing relative block rotations in the reference plane. The system preserved then some non-constrained degrees of freedom (free body). Real dimension of the hinge were considered, i.e., hinge was not simulated like a single point pivot. The FO element was simulated as an 80 μm diameter solid cylindrical rod (a pre-tensioned wire allows holding this hypothesis), with a Young modulus of 70GPa (glass material). The morphing rib structure was modeled by means of tetrahedral elements (see Fig. 5, detail of a hinge connecting two blocks). No friction was considered in the structural system. Relative rotations are expected to be in the range of +/- 5 °. (0.03 rad). α_0 was fixed to 160°. Some results comparing analytical and numerical predictions are reported in Fig. 6. The reported analysis refers to a rotating block, forced to move from 1 to 5 degrees with a 1° step. At each step, the strain along the fiber and the hinge rotation were computed. The deviation among output and estimated rotations (from strain info between 0.2 and 3%) are reported in Table 1.

It is worth to note that the results obtained through the analytical model do not take into account of the flexibility of the supporting structure; this because the analytical model is based only on geometric considerations.

4.2 Hinge rotation from experimental strain measurements

A simple proof of concept was realized verifying the numerical results and prove the idea's validity. A single-hinged rib and a preliminary sensing device demonstrator were manufactured. FBG was installed at the top of the sensor system, in order to magnify hinge rotation effects. FBG characteristic wavelength increased or decreased as a result of contraction or expansion, correlated to a negative or positive relative rotation. In the computations, a negative rotation was assumed if the blocks approached each other, otherwise positive. In the test, a single FBG was used to monitor the rotation angle, with no temperature compensation. The main sensors characteristics are reported in Table 2:

In Fig. 7, some details of the experimental setup are shown. On the left, the complete setup is presented. The Bragg wavelengths were measured by means of a commercial FBG interrogation system (Micron Optics sm130-700) based on a fiber Fabry–Pérot tunable filter, with a precision of 1 pm (www.smartfibres.com). In the bottom part of the same picture, a dummy wooden instrumented morphing rib can be seen. A zoom of the region where the introduced sensor system is installed, is presented on the right side. In order to detect the rotation angle over a graduated scale, a needle was fixed on one sensor component. This served for both measurement and calibration aims.

The experimental test respected the following logic. Two rigid blocks were considered, hinged to each other. One of these blocks was clamped. The structural system resulted then into a plane, SDOF kinematic chain. After the FO was preloaded and driven to an established position, a step load was imposed. Load increase was stopped as the needle pointed at 1°. The strain was then recorded and the configuration left relaxing for few minutes, in order to avoid any dynamic contributions. This operation was repeated for steps of 1 till 5° position was reached (5 steps).

Table 1 Analytical and numerical strain error estimation

(degree)	1	2	3	4	5
Analytical - rigid (geometrical) simulation (ε)	0,001658	0,003240	0,004745	0,006174	0,007527
FEM – flexible model simulation (ε)	0,001575	0,003150	0,004725	0,006300	0,007876
(*) Abs deviation (ε)	0,008	0,009	0,002	0,013	0,035
(**) Abs deviation (%)	5,27	2,86	0,42	2,00	4,43

*computed as difference between analytical and FEM outcomes

**% deviation with respect to the analytical values

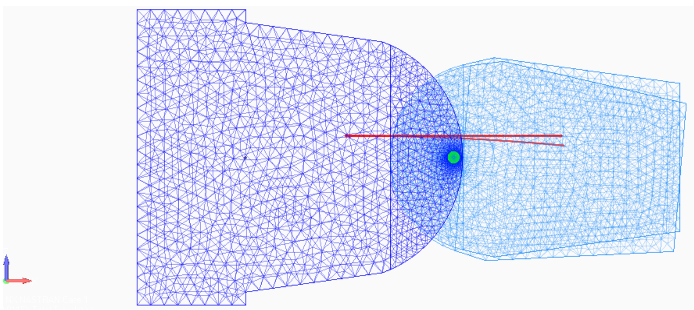

Fig. 5 FEM sketch of the sensorized hinge; deformed configuration with angle of rotation of 5 degree

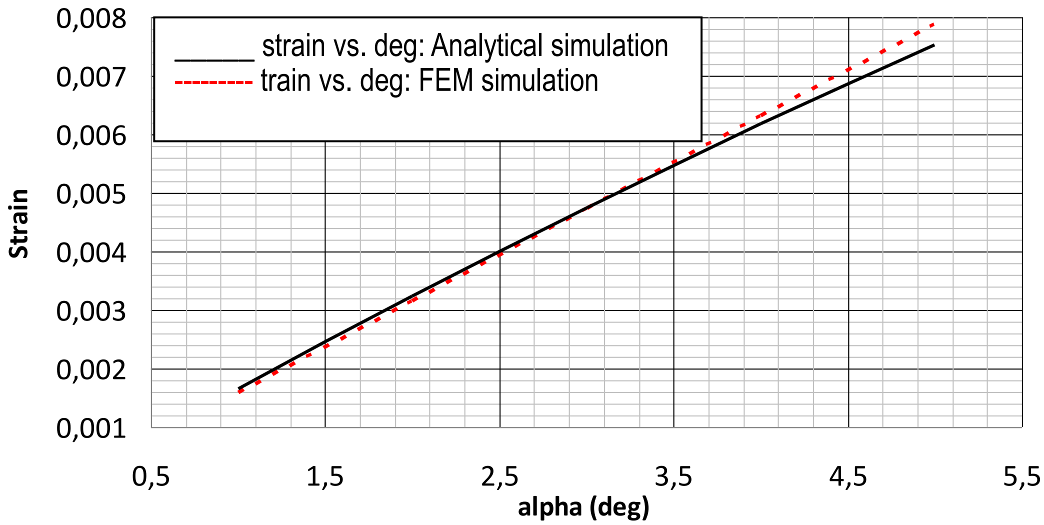

Fig. 6 Analytical and numerical comparison. Straight line: Analytical approach, Dotted line: finite element approach

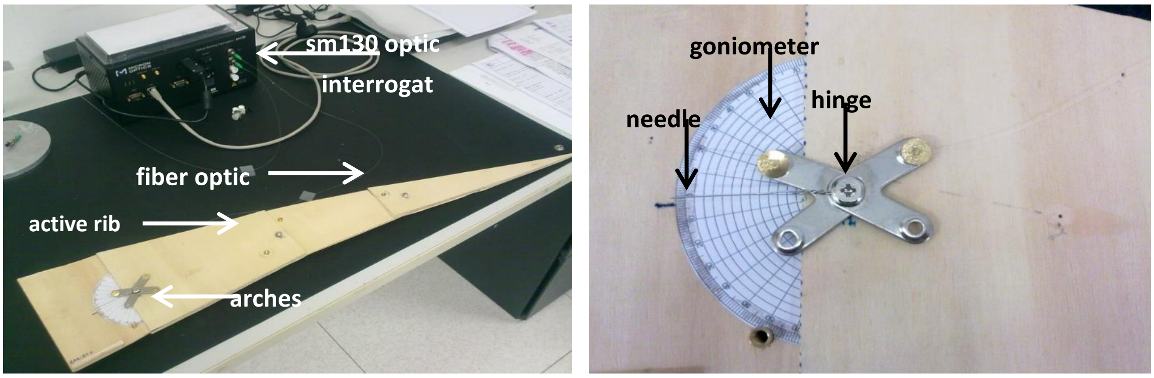

Fig. 7 Experimental test measurements – Strain time history at the hinge location following rib elements rotation

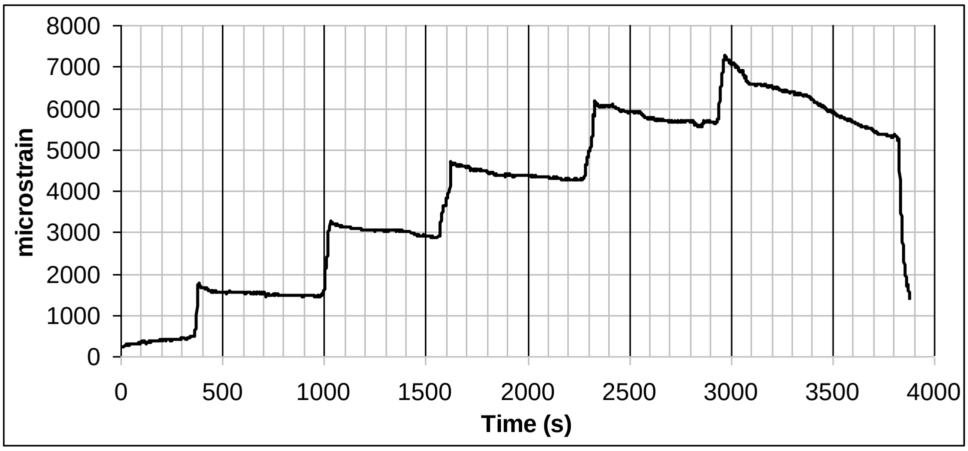

Fig. 8 Experimental test measurements – Strain time history at the hinge location following rib elements rotation

Table 2 Fiber optics sensor main characteristics

SENSOR SPECS	
Fiber type	Single mode
Number of FBG per rib	1
Position of the FBG	Close to the hinges
FBG sensitivity	1.20 pm/με
Fiber diameter (naked)	80 μm

An example of the achieved results is reported in Fig. 8. The graph reports the time history of the needle position as the rib elements are forced to rotate from 0 to 5 with 1° step. Overall test duration lasted about 4 thousands sec (quasi-static motion). The slow motion of the optical fiber, in turn related to a slow relaxation of the fiber itself and a slow sliding among its clamps, justifies the slow decay present in the time history. This aspect should not influence dynamics up to 1 Hz. The step fall at the end of the plot indicates the final load release. No breaks occurred in the fiber, in spite of the very high strain values achieved (around 1%). A good repeatability did show.

The analytical model results and the experimental outcomes were compared in Table 3 and Fig. 9.

The absolute and the % absolute deviations between numerical and experimental data kept lower than 346 με and 4.82%, respectively; these deviations were found for the maximum angle considered (5°). The experimental curve plotted in Fig. 9 resulted to be slightly lower than the numerical one and with a different slope; this discrepancy is caused by the aforementioned fiber relaxation due to the free-paly angles among the scissors arms and to the non-ideal rigidity of the fiber constraint.

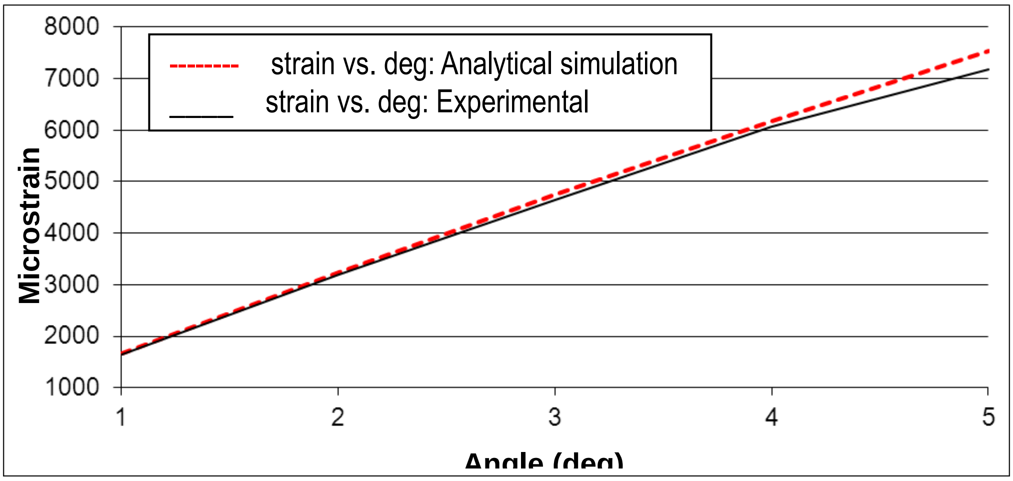

Fig. 9 Comparison of experimental vs. analytical strain measures

Table 3 Comparison of experimental vs. analytical strain measures

α (degree)	1	2	3	4	5
Time (s)	390	1030	1610	2320	2980
Analytical (με)	1658	3240	4745	6174	7527
Experimental (με)	1648	3190	4651	6079	7181
(*) Abs deviation (με)	10	50	94	95	346
(**) Abs deviation (%)	0,61	1,57	2,02	1,56	4,82

*computed as difference between analytical and FEM outcomes
**% deviation with respect to the analytical values

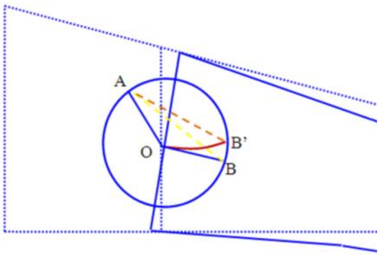

(a) complete concept

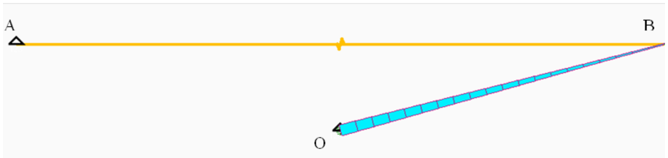

(b) finite element representation: elastic element – blue; optical fiber –yellow

Fig. 10 Qualitative effects of the elastic arches

4.3 Augmented arches device

In the current configuration, the measurable strain range coincides with the strain limit of the FO itself, the only element to absorb deformation. For suitable fiber layouts, this implies a maximum rotation angle of about 5°. If an additional elastic component is introduced the strain is partitioned between the elastic component itself and the sensing element and the above limits can be easily overcome. The elastic arches could for instance work according to the schematic of Fig. 10(a): because of the OB arm elasticity, its extremity moves from B to B', then reducing the inner FO strain. This alleviation can be controlled by a proper structural design of the elastic segment.

5. Design and optimization strategy

Many parameters affect the elastic arches behavior, both geometrical and physical; among them, its thickness, width and length as well as the selected material stress and strain limits, play a fundamental role. All these variables should be properly taken into account in order to come to an optimised design. A dedicated finite element model, Fig. 10(b), was realized, able to describe the elastic behavior of the proposed arches, with specific reference to its moving segment – OB in Fig. 10(a). The elastic arm was simulated through 20 beam elements; a simple spring represented the fiber, because of its simple 1D behavior. In the picture, a possible thickness distribution is qualitatively shown. A rotation equal to the deflection of the downward rib piece was imposed to the root of the elastic element (point O).

Referred layout constrains the segment length to 61 mm. The width gives just a linear contribution and is then fixed to a reference value. Material characteristics can be fixed as well at the beginning of the process.

The optimization process was constituted by two main phases: in the first one, a genetic approach was adopted to identify configurations able to guarantee a strain detection of 2000±50 $\mu\varepsilon$ for an imposed rotation of 5°; this guaranteed the possibility of identifying configurations characterized by the same sensitivity level within the range of (0 – 2000 $\mu\varepsilon$); in the second phase, the configurations previously selected were further filtered, with the aim of finding configurations exhibiting larger measurement ranges, better performance in terms of structural stress/strain level and a better linearity.

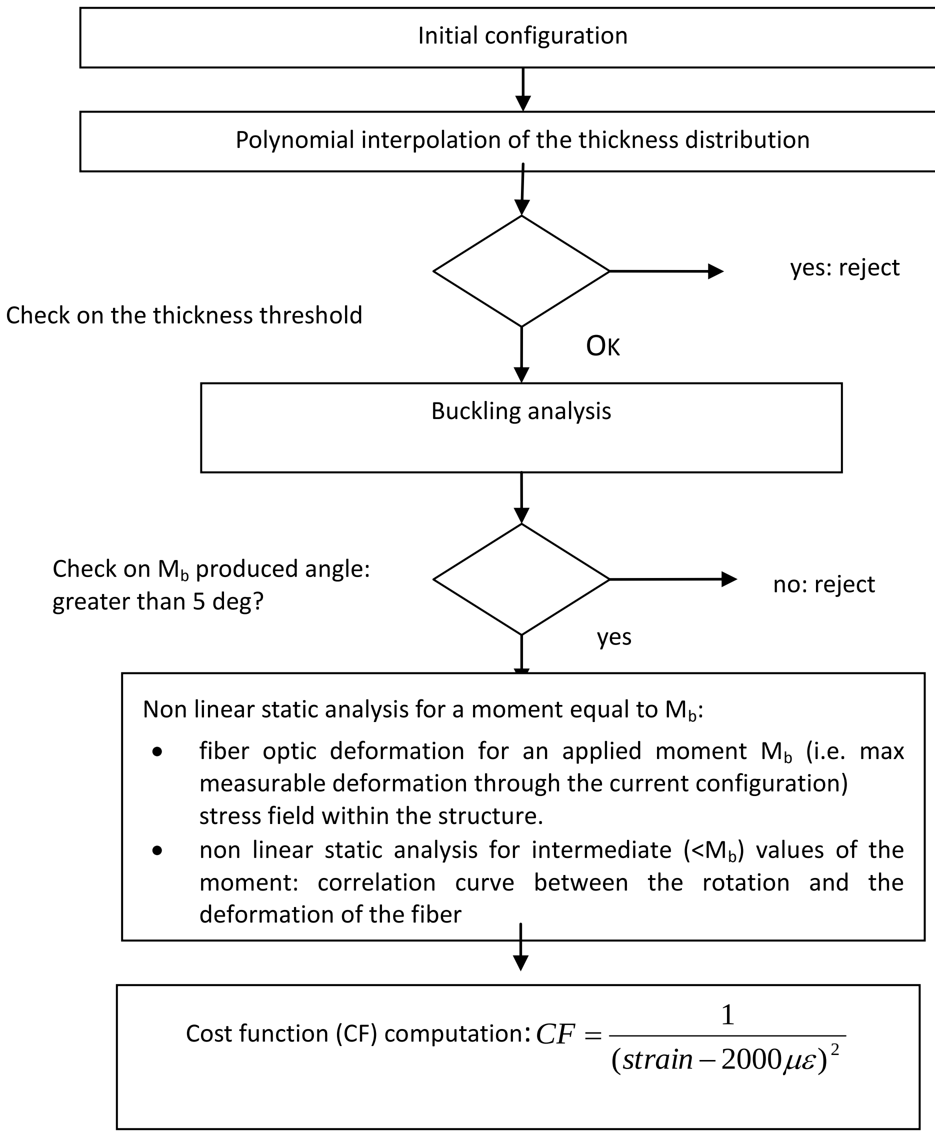

Fig. 11 Optimization flow chart

5.1 First phase of the optimization

For this phase, a dedicated constrained optimization algorithm was implemented, aimed at pointing out the best thickness distribution vector, defined at a certain pre-determined stations (namely, 0, 25, 50, 75, 100% length). As known, genetic algorithms are routines that make a given solution or set of solutions to evolve till convergence, using step instead of continuous variations (Russel and Norving). The logic behind is somehow linked to the evolutionary living systems theory and that is where their name come from. This kind of algorithm is probabilistic and some care should be devoted to avoid premature convergence and to improve results reliability. The most obvious way is to make runs starting from different sets of individuals (solutions) and compare the final output (sub-optimal solutions).

Individuals are made of strings representing the thickness vector, as defined before. The initial population is randomly generated. The resulting thickness law is interpolated by a polynomial curve, to prevent stress accumulations due to geometric discontinuities. A check is then performed to verify that the interpolation process does not lead to unacceptable values: for instance, lower than a fixed threshold – 0.4 mm.

The selection is performed on the basis of geometrical buckling and material stress / strain limits and adopting the inverse of the deviation from 2000 $\mu\varepsilon$ as cost function. In practice (see flowchart in Fig. 11) a buckling analysis is carried out on each configuration, to compute the induced rotation producing instability within the arm. The rotation obtained by Mb is then computed through a non-linear static analysis. If it results greater than 5°, fiber strain and structural stress field information are stored. Further non-linear analyses for intermediate moments are carried out to plot rotation – strain and stress curves. The optical fiber strain is finally computed at a rotation of 5° and compared through the cost function to the reference one (2000 $\mu\varepsilon$).

5.2 Second phase of the optimization

In the specific case, 20 initial populations were considered, each made of 50 individuals and 20 configurations meeting design constraints were selected. As already mentioned, coherently with the adopted cost function, all the configurations exhibit a very similar sensitivities within 0 – 2000 $\mu\varepsilon$.

The second optimization level was then implemented, with the aim of identifying configurations with better performance in terms of measurement range and stress/strain level and linearity of the rotation – strain law.

To this purpose, the 20 individuals were compared with each other on the basis of the maximum measurable angle, this one assumed to be the lowest among the rotations causing buckling or structural failure. A max allowable deformation of +/-4000 $\mu\varepsilon$ was assumed for the optical fiber; this value is a typical range value for pre-stressed fibers and compatible with typical fatigue life requirements (about 10 millions of cycles per ±5000 $\mu\varepsilon$) (http://www.smartfibres.com/FBG-sensors). For the structure an allowable stress of 300 MPa was considered; finally also the linearity of the sensor law was appreciated.

Dedicated parameters were thus defined to weight the configurations

- Angle range parameter, relating the achieved rotation angle for each configuration (current rotation) and the max recorded value (max rotation)

$$angle \quad range \quad parameter = \frac{current \quad rotation}{\max \quad rotation} \tag{10}$$

- Safety margin parameters, expressing the materials safety limits satisfaction:

$$fiber \quad strain \quad parameter = 1 - \frac{fiber \quad strain}{4000\mu\varepsilon} \tag{11}$$

$$structural \quad stress \quad parameter = 1 - \frac{structure \quad stress}{300MPa} \tag{12}$$

- System linearity parameter:

$$linearity \quad parameter = 1\% - \sqrt{\frac{res}{n}} \tag{13}$$

being res and n the summation of the squared residual related to the single individual and the number of samples, respectively. In Fig. 12 the computation of the residual between a curve and its least square line is provided

Eq. (13) in practice poses the deviation of 1% as upper limit of the scale; lower values, in fact, do not represent a serious problem for the measure, being the typical experimental accuracy of the optical interrogators higher.

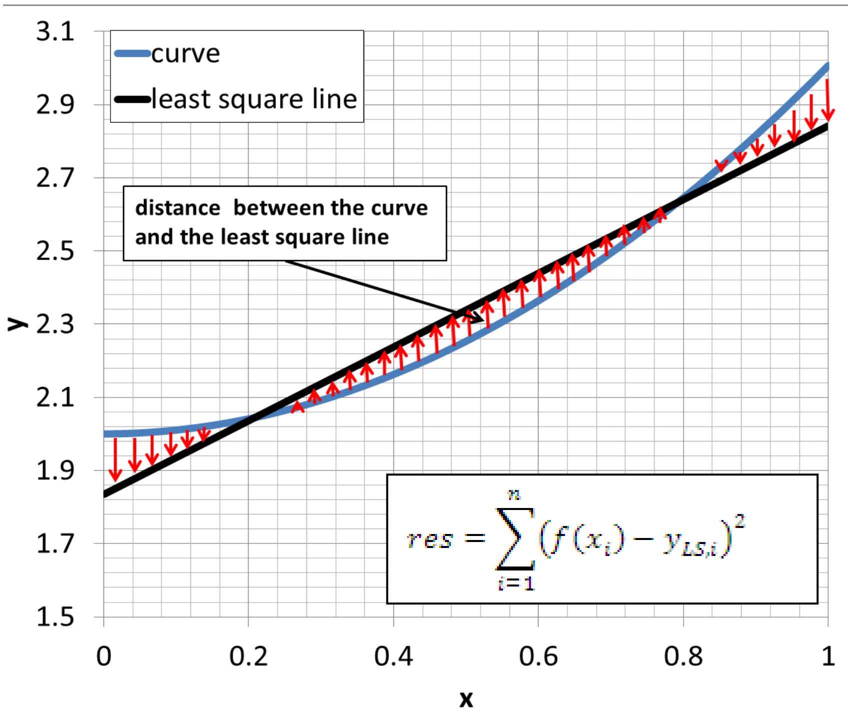

Fig. 12 Example of residual computation between a non-linear function, f(x), and the corresponding lest square line

6. Results

The output of the first phase of the optimization was represented by a set of 20 individuals each one assuring a strain measure of 2000 με for a rotation of 5°.

During the selection (second phase) the individuals were grouped in clusters of 5 and compared through radar graphs, reporting the angular, the safety and the linearity parameters. This instrument allowed having an immediate, visual idea of the different performances. The selected four individuals where finally compared, (Fig. 13), through the same process. The solution N.20 (bold violet line) proved to be the best compromise among the considered parameters. The corresponding thickness distribution is illustrated (Fig. 14). A linearized version of this distribution (more convenient from a manufacturing point of view), obtained by drawing the tangents at the edges of the thickness curve, was also presented in this graph (blue curve). The performance of this latter configuration was also reported (Fig. 15). In the linearized case the optical fiber resulted less loaded; however it is worth to note that, differently from the optimized case, the linearized one did not meet the condition of 2000 με at 5°. Also slightly worse performance in terms of linearity were found out with respect the optimized configuration.

The main performances of the rigid, optimized and linearized arms were finally summarized in table 4. Both flexible (optimized and linearized) configurations exhibited a wider measurement range than the rigid one (about 12.5 vs. 5°). The strain level within the optical fiber at the max angle rotation resulted dramatically lower (about 4000 against 7500 με, this latter referring to the rigid case for a rotation of 5°). This is coherent with the fact that the flexible arms cooperate in absorbing loads and thus alleviate the optical fiber. Also the weight resulted favorably diminished of about 10 times. This aspect plays a critical role in case of networking use of this kind of sensor; e.g., for a massive use of 1000 items, the weight safe is of 5 against 0.5 kg. An unavoidable consequence is fiber optic elastic sensor sensitivity reduction, following the strain levels decrease. Finally, the elastic architecture leads to a greater linearity level of the rotation-strain curve, as proved by the residuals computation with respect to the line of least squares. It is however worth to be noted that for all the configurations (rigid, flexible optimized and linearized) the non-linearity level proved to be lower than 1% of the maximum strain level (4000 με).

A comparison of the rotation vs. stress and strain curves is provided in Fig.15 for both the optimized and linearized configurations.

Table 4 Main characteristics of the flexible sensor and comparison with the rigid one

	Flexible Optimized	Flexible Linearized	Rigid	Upgrade/Down grade (optimized elastic vs. rigid)
Max measurable rotation (°)	12.5	12.4	5.0	U
Deformation of the optical fiber at 5 ° (με)	1980	1250	7527	U
Weight of the structural part (g)	0.49	0.44	5.0	U
Sensitivity (mdeg/με)	2.5	4.0	0.63	D
Mean deviation from linearity *(%)	0.88	0.83	0.48	U

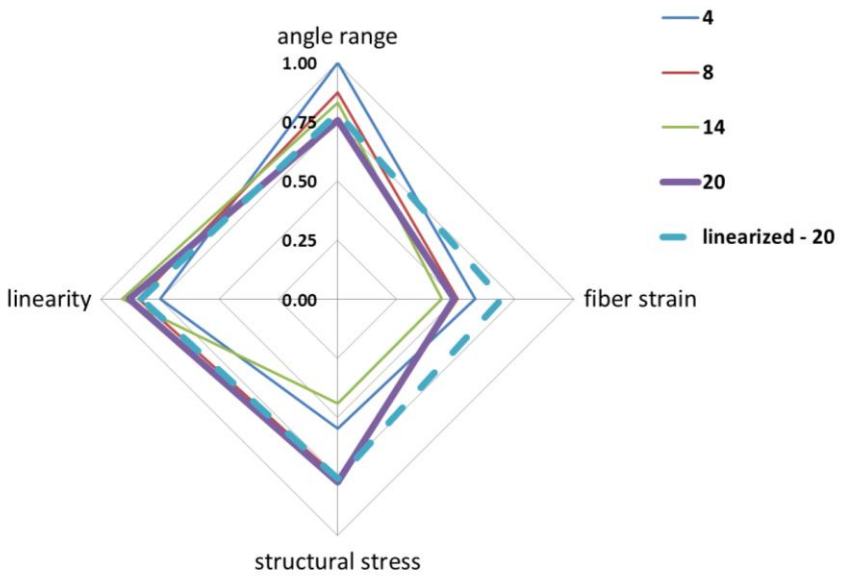

Fig. 13 Comparison of the 4 selected individuals

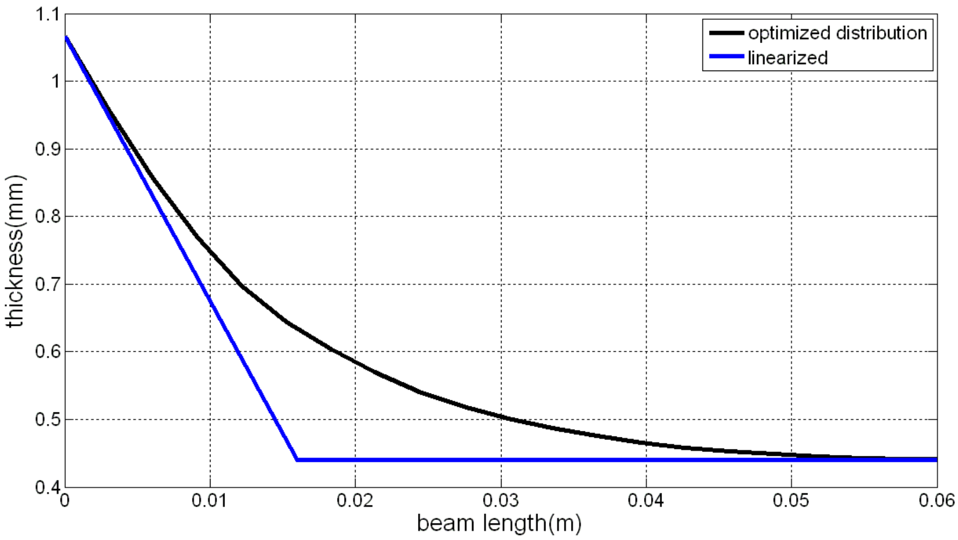

Fig. 14 Optimal thickness distribution

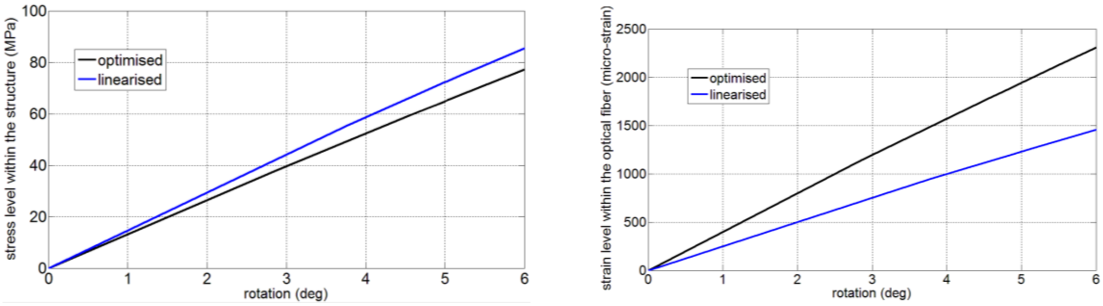

(a) structural stress (b) optical fiber deformation vs. rotation

Fig. 15 Quantitative effects of the optimised arches

5. Conclusions

An innovative structural sensor, FO-based, was herein introduced. The sensor system is herein proposed to monitor the local hinge rotation of the multi-body skeleton of the referred ATE structure. Moreover, dealing with morphing structures, large deformations are expected and a certain modulation has been necessary to keep the measured strain inside the permissible measure range.

The mechanical principle of a sensing device consisting of two arches hinged at their midpoint has been introduced. At a certain point of the top, notches clamped FO to reveal extension deformation. Nevertheless both compression and extension deformation layout can be also used, in this way sensor sensitivity and dynamic measurement range could be improved by using a simultaneous interrogation of two sensors. This last architecture would also allow self-compensating temperature variations.

Referring to the adaptive trailing edge, made of several rigid parts each rotating with respect to the others, rib excursions have been considered in the range up to 5°. The analytical relation between chord-wise strain and the hinge rotation has been found. Analytical results have been confirmed by finite element computations.

Experimental test results are presented, using a simple but representative setup. A step load has been imposed; load increase has been stopped as the needle pointed each degree from 1 to 5. The strain has been then recorded and the configuration left relaxing for few minutes, in order to avoid any dynamic influence.

A good correlation among data can be appreciated still being some discrepancies. The slow motion of the optical fiber, in turn related to a slow relaxation of the fiber itself and a slow sliding among its clamps, justifies the slow decay present in the time history. This aspect should not influence dynamics up to 1 Hz. No breaks occurred in the fiber, in spite of the very high strain values achieved (around 1%).

Finally, with the aim of improving the performance of the sensor system, the structural elasticity has been taken into account. A dedicated optimization process has been carried out to identify the best configuration of the structural sensor support that could guarantee a wider measurement range and a more linear sensor law. Both flexible (optimized and linearized) configurations exhibited a wider measurement range than the rigid one (about 12.5 vs. 5°). The strain level within the optical fiber at the max angle rotation resulted dramatically lower (about 4000 against 7500 $\mu\varepsilon$, this latter referring to the rigid case for a rotation of 5°). Also the weight resulted favorably diminished of about 10 times. An unavoidable consequence has been fiber optic elastic sensor sensitivity reduction, following the strain levels decrease. Finally, the elastic architecture led to a greater linearity level of the rotation-strain curve, as proved by the residuals computation.

Acknowledgments

The presented research has been partially funded the European Union Seventh Framework Programme (FP7/2007- 2013) under Grant Agreement n° 284562 (SARISTU Project).

The authors would express their gratitude to Mr. Antonio Alfano of University of Naples “Federico II” for his contribution in the realization of the experimental setup assessment.

References

Ameduri, S., Brindisi, A., Tiseo, B., Concilio A. and Pecora, R. (2012), “Optimization and integration of shape memory alloy (SMA)-based elastic actuators within a morphing flap architecture”, *J. Intel. Mat. Syst. Str.*, **23**(4), 381-396, 2012. DOI: 10.1177/1045389X11428672.

Ciminello, M., Concilio, A., Flauto, D. and Mennella, F. (2013), “FBG sensor system for trailing edge chord-wise hinge rotation measurements”, *SPIE* 8692, Sensors and Smart Structures Technologies for Civil, Mechanical, and Aerospace Systems; doi: 10.1117/12.2012017.

Duncan, P.G., Jones, M.E., Shinpaugh, K.A., Poland, S.H., Murphy, K.A. and Claus, R.O. (2003), “Optical fiber pressure sensors for adaptive wings”, *Proc. SPIE*, **3042**, 320-331.

Hui, Y., Xiufeng, Y., Zhengrong, T., Ye, C. and Ailing, Z. (2011), “Temperature-indipendent rotational angle sensor based on fiber Bregg grating”, *IEEE Sens. J.*, **11**(5), 1233-1235.

Jones, M.E., Duncan, P.G., Crotts, R., Shinpaugh, K., Grace, J.L., Murphy, K.A. and Claus, R.O. (2006), “Multiplexing optical fiber-based pressure sensors for smart wings”, *Proc. SPIE*, **2838**, 230-236.

Kirkendall, C.K. and Anthony, D.A. (2007), “Overview of high performance fibre-optic sensing”, *J. Physics D: Appl. Phys*., **37**(18), 197-216.

Liu, D., Ngo, N.Q., Tjin, S.C. and Dong, X. (2004), “A dual-wavelength fiber laser sensor system for measurement of temperature and strain”, *IEEE Photon. Technol*., **19**(15), 1148-1150.

Lee, J.R., Ryu, C.Y., Koo, B.Y.., Kang, S.G., Hong, C.S. and Kim, C.G. (2003), “In-flight health monitoring of a subscale wing using a fiber Bragg grating sensor”, *Smart Mater. Struct*. **12**(1), 147-155 .PII: S0964-1726(03)56154-7.

Mohanna, Y., Saugrain, J.M., Rousseau, J.C. and Ledoux, P. (2002), “Relaxation of internal stresses in optical fibers”, *J. Lightwave Technol*., **8** (12), 1799-1802 , doi:10.1109/50.62873.

Pecora, R., Amoroso, F. and Lecce, L. (2012), “Effectiveness of wing twist morphing in roll control”, *J. Aircraft*, **49**(6), 1666-1674.

Pecora, R., Barbarino, S., Concilio, A., Lecce, L. and Russo, S. (2011), “Design and functional test of a morphing high-lift device for a regional aircraft”, *J. Intel. Mat. Syst. Str.*, **22**(10), 1005-1023, 2011. DOI: 10.1177/1045389X11414083.

Russel, S. and Norvig, P., *Artificial Intelligence*, Prentice Hall International, ISBN 88-7750-406-4

Website links, http://www.saristu.eu/project/activities/as-02-structural-tailoring-of-wing- trailing-edge-device/

Website links, http://www.smartfibres.com/FBG-interrogators

Website links, http://www.smartfibres.com/FBG-sensors

BS